# Robust and Fast Vessel Segmentation via Gaussian Derivatives in Orientation Scores

Jiong Zhang[1](✉), Erik Bekkers[1], Samaneh Abbasi[1], Behdad Dashtbozorg[1], and Bart ter Haar Romeny[1,2]

[1] Department of Biomedical Engineering, Eindhoven University of Technology, Eindhoven, The Netherlands
{J.Zhang1,E.J.Bekkers,S.Abbasi,B.Dasht.Bozorg,B.M.TerHaarRomeny}@tue.nl
[2] Department of Biomedical and Information Engineering, Northeastern University, Shenyang, China

**Abstract.** We propose a robust and fully automatic matched filter-based method for retinal vessel segmentation. Different from conventional filters in 2D image domains, we construct a new matched filter based on second-order Gaussian derivatives in so-called orientation scores, functions on the coupled space of position and orientations $\mathbb{R}^2 \rtimes S^1$. We lift 2D images to 3D orientation scores by means of a wavelet-type transform using an anisotropic wavelet. In the domain $\mathbb{R}^2 \rtimes S^1$, we set up rotation and translation invariant second-order Gaussian derivatives. By locally matching the multi-scale second order Gaussian derivative filters with data in orientation scores, we are able to enhance vessel-like structures located in different orientation planes accordingly. Both crossings and tiny vessels are well-preserved due to the proposed multi-scale and multi-orientation filtering method. The proposed method is validated on public databases DRIVE and STARE, and we show that the method is both fast and reliable. With respectively a sensitivity and specificity of 0.7744 and 0.9708 on DRIVE, and 0.7940 and 0.9707 on STARE, our method gives improved performance compared to state-of-the-art algorithms.

**Keywords:** Retinal vessel segmentation · Matched filter · Gaussian derivatives · Orientation scores · Crossing preservation · Micro-vasculature

## 1 Introduction

The analysis of retinal images, especially retinal blood vessels, provide useful information for the early diagnosis of systematic and eye-related diseases, such as diabetes, hypertension, and arteriosclerosis [1]. The changing geometric properties of vessels need to be quantified as important biomarkers (as humans are not good at this), and then analyzed to assist the ophthalmologists. To this end, a vascular tree needs to be segmented from the retinal image to support clinical diagnosis and treatment planning. In this work, we propose a robust, efficient and unsupervised vessel segmentation approach. Our method provides a sound basis for the quantitative analysis of large data sets, e.g. in a screening setting.


V. Murino and E. Puppo (Eds.): ICIAP 2015, Part I, LNCS 9279, pp. 537–547, 2015.
DOI: 10.1007/978-3-319-23231-7_48

In a general sense, conventional segmentation approaches can be divided into three categories: classifier-based [2,3], tracking-based [4] and filter-based [5–7]. Classifier-based methods rely on a prior labor-intensive process to label training samples, which are pixels with given feature vectors and known answers for learning a model. E.g., Soares et al. [2] extract a feature vector for a supervised classification from the pixel intensity and matched filter responses. Tracking based methods iteratively expand connected vessel models starting from detected seed points. These methods heavily rely on both the correct detection of seed points, and robustness of the iterative tracking scheme [4,8].

Other algorithms [5–7,9–11], including ours, are based on maximizing the filter response of the gray-level profile of the vessel cross-section. These approaches are generally faster and simpler than supervised methods. A Gaussian cross-section model was firstly proposed by Chaudhuri et al. [12] to describe the intensity variations of a vessel profile. Mendonca and Campilho [13] employed differential filters to detect vessel centerlines followed by morphological operators for vessel segmentation. Krause et al. [9] proposed a fast and accurate retinal vessel segmentation method in a higher dimension, in which vessels are detected through convolution with the second-order differential operator of the local Radon transform. In our work, we follow a similar approach of processing image data in a higher dimensional domain, but instead of using the local Radon transform, we rely on the formal group-theoretical frame-work of orientation scores [4,14,15]. Additionally, we exploit a multi-scale approach using rotation invariant Gaussian derivatives.

The theory of invertible orientation scores is inspired by the orientation-selective property of cortical hypercolumns in the primary visual cortex [16]. Invertible orientation scores are constructed by lifting 2D images to 3D functions on the roto-translation group $SE(2)$, an extended Lie-group domain of positions and orientations $\mathbb{R}^2 \rtimes S^1$. In the additional third orientation dimension, elongated structures of 2D images are disentangled into different orientation planes separately without tampering data-evidence, see Fig. 1. Here, we will develop multi-scale matched filters that live in the domain of an orientation score. By locally matching the vessel profile to the second order Gaussian differential operator perpendicular to the corresponding orientation, the vessel intensity can be enhanced accordingly. In the validation phase, we show that the proposed method not only gives improved performance on the major parts of the retinal vasculature with a competitive speed, but also is capable of dealing with difficult cases such as strong central arterial reflex, crossings, highly curved vessel parts, closely parallel and tiny vessels.

The remainder of this article is organized as follows: In Section 2 we provide the theory of invertible orientation scores on $SE(2)$, the left-invariant Gaussian derivatives and the constructed multi-scale matched filters. In Section 3 we validate the performance of our method with special attention on handling difficult structures. We conclude our paper in Section 4.

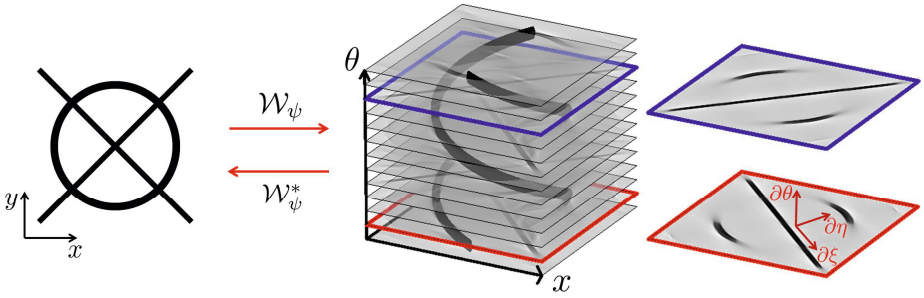


**Fig. 1.** Exemplary image with circle and cross, and corresponding orientation score.

## 2 Theory

In this section, we will firstly give details of the domain where we exploit left-invariant operators. Then we will explain why we need to keep left-invariance on that domain, and how to build Gaussian derivatives with left-invariance property.

### 2.1 Invertible Orientation Scores on SE(2)

**The Euclidean Motion Group $SE(2)$.** The domain $\mathbb{R}^2 \rtimes S^1$ of an orientation score can be identified with the group $SE(2)$, equipped with group product

$$gg' = (\mathbf{x}, \theta)(\mathbf{x}', \theta') = (\mathbf{x} + \mathbf{R}_\theta \cdot \mathbf{x}', \theta + \theta'), \quad \textit{for all} \quad g, g' \in SE(2), \tag{1}$$

with $\mathbf{R}_\theta = \begin{pmatrix} \cos\theta & -\sin\theta \\ \sin\theta & \cos\theta \end{pmatrix}$ a counter clockwise rotation over angle $\theta$.

**Invertible Orientation Scores.** An orientation score $U_f : SE(2) \to \mathbb{C}$ is defined on the group $SE(2)$. The transform from an image $f$ to an orientation score $U_f := \mathcal{W}_\psi f$ is achieved via an anisotropic convolution kernel $\psi \in \mathbb{L}_2(\mathbb{R}^2)$:

$$U_f(\mathbf{x}, \theta) = (\mathcal{W}_\psi[f])(\mathbf{x}, \theta) = \int_{\mathbb{R}^2} \overline{\psi(\mathbf{R}_\theta^{-1}(\mathbf{y} - \mathbf{x}))} f(\mathbf{y}) d\mathbf{y}, \tag{2}$$

where $\mathcal{W}_\psi$ denotes the transform between image $f$ and orientation score $U_f$. Here we choose cake wavelets[1] [4] for $\psi$. Exact reconstruction is obtained by

$$f(\mathbf{x}) = (\mathcal{W}_\psi^*[U_f])(\mathbf{x}) = \left( \mathcal{F}_{\mathbb{R}^2}^{-1} \left[ M_\psi^{-1} \mathcal{F}_{\mathbb{R}^2} \left[ \frac{1}{2\pi} \int_0^{2\pi} (\psi_\theta * U_f(\cdot, \theta)) d\theta \right] \right] \right)(\mathbf{x}), \tag{3}$$

for all $\mathbf{x} \in \mathbb{R}^2$, where $\mathcal{F}_{\mathbb{R}^2}$ is the unitary Fourier transform on $\mathbb{R}^2$ and $M_\psi$ is given by $M_\psi(\boldsymbol{\omega}) = \int_0^{2\pi} |\hat{\psi}(\mathbf{R}_\theta^{-1}\boldsymbol{\omega})|^2 d\theta$ for all $\boldsymbol{\omega} \in \mathbb{R}^2$, with $\hat{\psi} := \mathcal{F}_{\mathbb{R}^2}\psi$, $\psi_\theta(\mathbf{x}) =$

[1] They are called 'cake' kernels, as they are constructed by dividing the Fourier domain in equal angular segments from the origin, like pieces of a cake.

$\psi(R_\theta^{-1}\mathbf{x})$. Well-posedness of the reconstruction is controlled by $M_\psi$ [4,15]. One important advantage of cake wavelets is that they cover all frequencies in the Fourier domain such that a stable inverse transform $\mathcal{W}_\psi^*$ is allowed to return to the image $f$.

### 2.2 Left-Invariant Gaussian Derivatives on Orientation Scores

**Left-Invariant Moving Frame of Reference.** See Fig. 2, all operators $\Phi$ on invertible orientation scores relate to the effective operator $\Upsilon := \mathcal{W}_\psi^* \circ \Phi \circ \mathcal{W}_\psi$ on the image domain. Euclidean-invariance of $\Upsilon$ is ensured by left-invariance of $\Phi$. This is a desirable property since we can keep all operations invariant with respect to translation and rotation. The left-invariance can be preserved if the operator $\Phi$ on orientation scores satisfies $\Phi \circ \mathcal{L}_g = \mathcal{L}_g \circ \Phi$ for all $g \in SE(2)$, with group representation $g \mapsto \mathcal{L}_g$ given by $\mathcal{L}_g U_f(g') = U_f(R_\theta^{-1}(\mathbf{x}' - \mathbf{x}), \theta' - \theta)$, for all $g = (\mathbf{x}, \theta), g' = (\mathbf{x}', \theta') \in SE(2)$. Therefore we should rely on the following frame of left-invariant derivatives acting on the domain $SE(2)$ of orientation scores:

$$\{\partial_\xi, \partial_\eta, \partial_\theta\} = \{\cos\theta\partial_x + \sin\theta\partial_y, -\sin\theta\partial_x + \cos\theta\partial_y, \partial_\theta\}, \tag{4}$$

where we use short hand notation $\partial_i = \frac{\partial}{\partial_i}$.

**Left-Invariant Gaussian Derivatives.** Suitable combinations of derivatives have been widely used to pick up geometric invariant structures/features like edges, ridges, corners and so on. However, obtaining derivatives directly is an ill-posed problem. Therefore, we regularize the orientation scores via convolutions with Gaussian kernels $G_{\sigma_s,\sigma_o}(\mathbf{x}, \theta) = G_{\sigma_s}(\mathbf{x})G_{\sigma_o}(\theta)$, with a $d-$dimensional Gaussian given by $G_\sigma(\mathbf{x}) = (2\pi\sigma^2)^{-d/2}\, e^{-\frac{\|\mathbf{x}\|^2}{2\sigma^2}}$, and where $\sigma_s$ and $\sigma_o$ are used to define the spatial scale $\frac{1}{2}\sigma_s^2$ and orientation scale $\frac{1}{2}\sigma_o^2$ of the Gaussian kernel. Note that $G_{\sigma_s} : \mathbb{R}^2 \to \mathbb{R}^+$ the spatial Gaussian distribution *must be isotropic* to preserve commutator relations of the $SE(2)$ group for scales $\sigma_s > 0$, i.e., to preserve left-invariance.

### 2.3 Scale-Invariant Matched Filters

It is well-known that the second-order Gaussian derivatives can be used to match vessel profiles for enhancement [9,17]. Here, based on the local coordinates system $\{\xi, \eta, \theta\}$ in the orientation score domain, we propose the second-order operator $\Phi_\eta^{\sigma_s,\sigma_o}(U_f) := \partial_\eta^2(G_{\sigma_s,\sigma_o} * U_f)$ perpendicular to the orientation of elongated structures for vessel detection. By applying isotropic Gaussian blurring spatially in $\xi$ and $\eta$ directions, as well as a small Gaussian blurring angularly in $\theta$ direction, we enforce structure smoothness on different orientation planes and information propagation along the vessel directions. Moreover, the variation of retinal vessel calibers requires a proper scale selection of second-order operators to match different vessel profiles. As studied by Lindeberg [18], the response of a derivative of Gaussian filter decreases as $\sigma$ increases. Therefore, a scale normalization factor

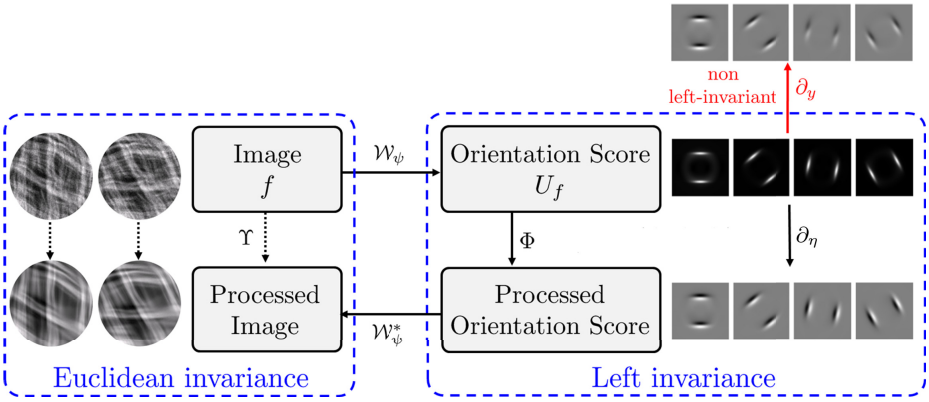


**Fig. 2.** Image processing via invertible orientation scores. Operators $\Phi$ on the invertible orientation score robustly relate to operators $\Upsilon$ on the image domain. Euclidean-invariance of $\Upsilon$ is obtained by left-invariance of $\Phi$. We show the relevance of left-invariance of $\partial_\eta$ acting on an image of a circle (as in Fig. 1) compared to action of the non-left-invariant derivative $\partial_y$ on the same image.

$\mu = \sigma_o/\sigma_s$ with physical unit 1/length is required to make the filter responses dimensionless and truly scale invariant. The angular scale $\sigma_o$ is a kept constant over all spatial scales and therefore does not affect extrema response. Thus our scale-normalized second-order matched filter can be written as:

$$\Phi^{\sigma_s,\sigma_o}_{\eta,\mathrm{norm}}(U_f) := \mu^{-2}\Phi^{\sigma_s,\sigma_o}_{\eta}(U_f) = \mu^{-2}\partial^2_\eta(G_{\sigma_s,\sigma_o} * U_f). \tag{5}$$

In the $SE(2)$-generalizations, the final image reconstruction from the multi-scale filtered orientation scores is obtained via

$$\Upsilon^{\sigma_s,\sigma_o}_{\eta}(f))(\mathbf{x}) := \max_{\theta_{i\in\{1,2,\ldots N_o\}}} \{\sum_{\sigma_s\in\mathcal{S}} \Phi^{\sigma_s,\sigma_o}_{\eta,\mathrm{norm}}(U_f)(\mathbf{x},\theta_i)\}, \tag{6}$$

where $N_o$ and $\mathcal{S}$ represents the number of orientations and the set of spatial scalings respectively, and the maximum filter response is calculated over all orientations per position.

## 3 Validation and Experimental Results

### 3.1 Settings

**Preprocessing.** Retinal images very often suffer from non-uniform illumination and varying contrast, which may affect the later detection process. Therefore we use the luminosity and contrast normalization proposed by Foracchia et al. [19]. The normalization radius for creating a disk-shaped filter is set as $r_{LC} = \frac{l_h}{30}$, where $l_h$ is the height of an image. Moreover, the strong brightness of the optic disk and pathologies in RGB retinal images will cause erroneous detection of

their boundary. So the morphological bottom-hat transform with respect to a range-7 square is used to decrease false positives.

**Threshold.** In this work, we employ a relatively simple strategy to define a global threshold value. Since our matched filters can obtain a high response only in vessel-like structures, we basically select the threshold value of different data sets according to their general percentage of vessel pixels. The first human observers of the DRIVE [20] and STARE [5] data sets marked around $(12.7 \pm 1.2)\%$ and $(10.4 \pm 2.0)\%$ pixels as vessels from 20 testing images respectively. In our experiments, we obtain the best results by setting the threshold value as 12.4% for the DRIVE database and 10.7% for the STARE database.

**Scales.** Generally, the maximum response of the second-order derivative occurs at $\sigma = r/\sqrt{2}$, where $r$ represents the radius of the vessel caliber [18]. The vessel calibers of the DRIVE and STARE data sets roughly range from 2 to 14 pixels. In our experiments, we sample the spatial scales $\sigma_s$ for both data sets as $\mathcal{S} = \{0.7, 1.0, 1.5, 2.0, 2.5, 3.5, 4.5\}$ with a small angular blurring $\sigma_o = \pi/5$. For the orientation score transformation we use $N_o = 36$ orientations sampled from 0 to $\pi$. In Fig. 3, we give segmentation examples on the DRIVE and STARE data sets based on our proposed method.

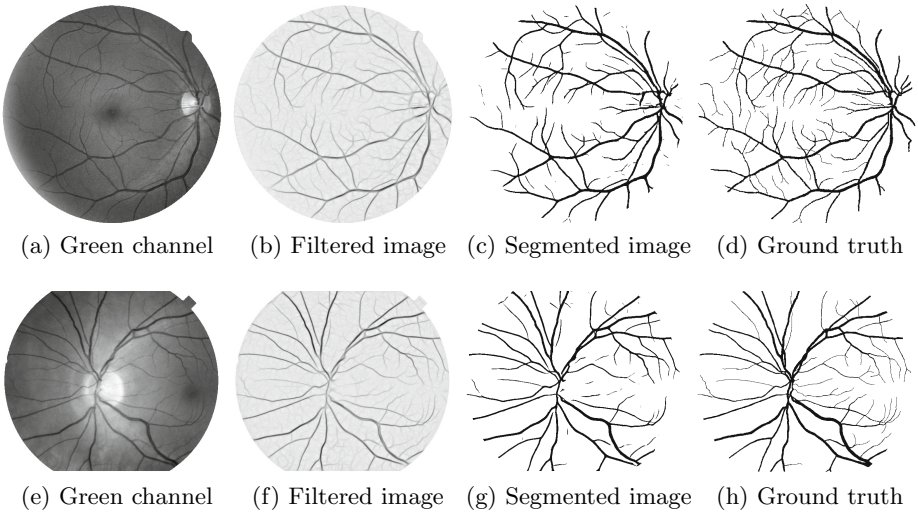

(a) Green channel (b) Filtered image (c) Segmented image (d) Ground truth

(e) Green channel (f) Filtered image (g) Segmented image (h) Ground truth

**Fig. 3.** Examples of automatic vessel segmentation on two images by the proposed approach. (a)-(d): An image from the DRIVE data set ($Sen = 0.8308$, $Spc = 0.9824$ and $Acc = 0.9635$). (e)-(h): An image from the STARE data set ($Sen = 0.8587$, $Spc = 0.9806$ and $Acc = 0.9676$).

### 3.2 Difficult Structures Preservation

Retinal vessel segmentation often suffers from difficult cases such as strong central reflex, crossings/bifurcations, highly curved vessel parts, closely parallel and tiny vessels. In order to investigate the influence of our proposed vessel enhancement in $SE(2)$, we compare this to multi-scale Frangi vesselness filtering in $\mathbb{R}^2$ [17], a frequently used method in vessel segmentation tasks. For the sake of equal comparison we substitute the filter $\Upsilon_{\eta}^{\sigma_s,\sigma_o}$ in our implementation with the Frangi vesselness filter, with the same preprocessing steps and scale settings as our approach. The best performance of the Frangi vesselness filter is obtained based on the $F_1 - score$ measure, which is the mean of precision and recall. As shown in Fig. 4 (a)-(c), the Frangi vesselness filter performs well on picking up parallel vessel structures, however, it has limitations to connect the low intensity vessel profiles of crossings and highly curved vessel parts. Missing of the central vessel parts due to the central reflex and partially merging segmentation of two closely parallel vessels can be seen in the results of the supervised segmentation method by Soares et al. [2], as shown in Fig. 4 (e) and (f). From Fig. 4 (g) and (h) we can see that the recently proposed B-COSFIRE filter [11] also suffers from difficult crossing cases. The proposed orientation score based multi-scale matched filters show much better structure preservation ability on these special cases, as illustrated in Fig. 4 (j)-(l). Quantitative results are tabulated in Table 1, and further discussed in Section 3.4.

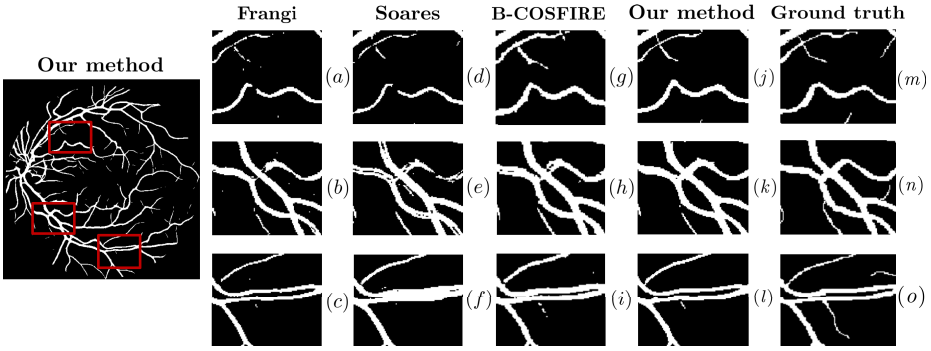


**Fig. 4.** Vessel segmentation results of our method in comparison with state-of-the-art methods on an image of the DRIVE database. (a)-(c), (d)-(f) and (g)-(i) respectively show the vessel segmentation results by the methods of Frangi et al. [17], Soares et al. [2] and B-COSFIRE filter [11] on 3 difficult cases: (a) high curvature change on low intensity vessel part and tiny crossing, (b) artery and vein crossing with central reflex and (c) closely parallel vessels; (j)-(l) show the results of our method, and (m)-(o) give the corresponding ground truth annotations by the human observer [20].

### 3.3 Validation of Vessel Calibers

To show the performance of our vessel detection approach on vessels of different calibers, particularly on small vessel width with 2-3 pixels, we validate the vessel

width distribution on the detected true positive pixels. The basic procedure is as follows: we assign to each ground truth pixel a vessel caliber value based on the vessel caliber of the closest centerline point. Caliber of centerline pixels are found via thinning and a distance transform on the ground truth segmentation.

In Fig. 5, we show the comparisons of true positive ratio (TPR) with respect to different vessel calibers on the STARE database. In order to make an equal comparison, we move along the ROC curves of the proposed matched filter approach such that we can compare the sensitivity at the same specificity level where other methods [2,11,17] achieve their best performance. In general, we can see that our method can not only outperform the others on large vessel calibers, but also can detect more tiny vessels with caliber 2-3 pixels. Although the supervised segmentation approach by Soares et al. [2] performs slightly better on vessel calibers with 8-10 pixels, our method gives a large increase in performance on small calibers with 2-5 pixels.

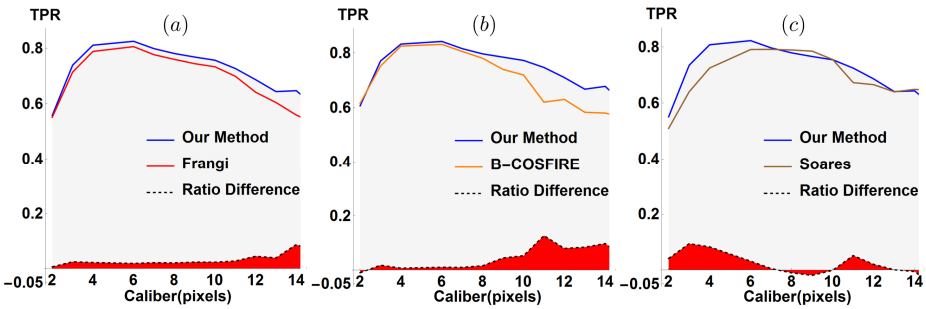


**Fig. 5.** Comparisons of the average true positive ratio (TPR) with respect to vessel calibers on the whole STARE database. The three figures show the comparison between our proposed method with (a) Frangi-vesselness filter [17], (b) B-COSFIRE filter [11], and (c) supervised segmentation by Soares et al. [2]. The bottom region with red color represents the true positive ratio differences.

### 3.4 Comparison with the State-of-the-Art

We validate our method on the public DRIVE and STARE data sets according to the aforementioned parameter settings from Section 3.1. In order to compare our method with other vessel segmentation algorithms, we use the performance measures: *Sensitivity* (*Sen*), *Specificity* (*Spc*) and *Accuracy* (*Acc*) to evaluate the classified pixels within the field of view (FOV). Table 1 shows the experimental results of different algorithms evaluated on the DRIVE and STARE data sets. The performance measures of the methods we compare come from their respective references.

We can see that our method leads to very good and competitive results in comparison to other supervised and unsupervised methods from the literature. Particularly, our method achieves a higher sensitivity level compared to other

algorithms. For the sake of equal comparison on sensitivity, we move along the ROC curves in order to validate the performance of our approach with respect to the best results achieved by other algorithms. As can be seen from Table 1, the two highest sensitivities on the DRIVE database are reported by B-COSFIRE filter [11] ($Sen = 0.7655$ and $Spc = 0.9704$) and Krause et al. [9] ($Sen = 0.7517$ and $Spc = 0.9741$). Our method can achieve a better sensitivity of 0.7761 and 0.7587 for the same specificity of the two methods respectively. Similarly, we can see from Table 1 that the two highest sensitivities for the STARE database are obtained by B-COSFIRE filter [11] ($Sen = 0.7716$ and $Spc = 0.9701$) and Frangi vesselness [17] ($Sen = 0.7540$ and $Spc = 0.9744$). Here based on our method we can reach to a significantly better result with sensitivities 0.7980 and 0.7743 for the same specificity of the two algorithms respectively.

**Table 1.** Segmentation results on the DRIVE and STARE data sets.

| | DRIVE | | | STARE | | |
|---|---|---|---|---|---|---|
| Method | *Sen* | *Spc* | *Acc* | *Sen* | *Spc* | *Acc* |
| **Our Method** | **0.7744** | **0.9708** | **0.9446** | **0.7940** | **0.9707** | **0.9511** |
| 2nd human observer | 0.7761 | 0.9725 | 0.9473 | 0.8949 | 0.9390 | 0.9354 |
| Matched filter [12] (1989) | 0.6168 | 0.9741 | 0.9284 | 0.6134 | 0.9755 | 0.9384 |
| Frangi [17] (1998) | 0.7460 | 0.9719 | 0.9418 | 0.7540 | 0.9744 | 0.9503 |
| Mendonca [13] (2006) | 0.7344 | 0.9764 | 0.9452 | 0.6996 | 0.9730 | 0.9440 |
| Soares [2] (2006) | 0.7332 | 0.9782 | 0.9466 | 0.7207 | 0.9747 | 0.9480 |
| MF-FDOG [10] (2010) | 0.7120 | 0.9724 | 0.9382 | 0.7177 | 0.9753 | 0.9484 |
| Marin [3] (2011) | 0.7067 | 0.9801 | 0.9452 | 0.6944 | 0.9819 | 0.9526 |
| MPMF [7] (2012) | 0.7154 | 0.9716 | 0.9343 | 0.7191 | 0.9687 | 0.9407 |
| Krause[9] (2013) | 0.7517 | 0.9741 | 0.9468 | - | - | - |
| B-COSFIRE [11] (2015) | 0.7655 | 0.9704 | 0.9442 | 0.7716 | 0.9701 | 0.9497 |

**Table 2.** Comparative analysis of running time for processing a DRIVE/STARE image.

| Method | Running time |
|---|---|
| **Our Method (Sequential Mode)** | 15 s |
| Mendonca [13] (2006) | 2.5 min |
| Soares [2] (2006) | 3 min |
| Marin [3] (2011) | 1.5 min |
| B-COSFIRE [11] (2015) | 10 s |

### 3.5 Speed Comparison

The proposed orientation score based multi-scale matched filters have the advantage of time-efficiency for real applications. The *Mathematica* implementation we

used for experiments takes less than 15s for segmenting an entire image from the DRIVE ($565 \times 584$ pixels) and STARE data sets ($700 \times 605$ pixels), on a personal computer with a 2 GHz processor. However, the computational speed can still be improved if we use a parallel mode to process multiple scales simultaneously. Comparative analysis of running time can be seen in Table 2.

## 4 Conclusion

In this paper, we have proposed a robust and efficient multi-scale and multi-orientation matched filter approach for retinal vessel segmentation. The filter is constructed by the left-invariant second-order Gaussian derivatives in the orientation score domain, where the vessel-like structures are disentangled into different orientations accordingly. With proper scale selection and simple parameter settings, the newly proposed method can match the vessel profile and maximize the filter response on multiple vessel calibers. After that, a global threshold value is defined to segment the filtered retinal image according to the general percentage of vessel pixels. The validation results show that the proposed matched filter not only gives improvement on global performance compared to most of the state-of-the-art segmentation schemes, but is also capable of dealing with generally difficult vessel structures. Last but not the least, the high computational efficiency of our method gives the potential of applying vessel segmentation on large data sets.

**Acknowledgments.** The research leading to these results has received funding from the China Scholarship Council (CSC) No. 201206300010. This work is also part of the NWO-Hé Programme of Innovation Cooperation 2013 No. 629.001.003 and the European Foundation for the Study of Diabetes/Chinese Diabetes Society/Lilly project.

## References

1. Ikram, M.K., Ong, Y.T., Cheung, C.Y., Wong, T.Y.: Retinal vascular caliber measurements: clinical significance, current knowledge and future perspectives. Ophthalmologica **229**(3), 125–136 (2013)
2. Soares, J.V.B., Leandro, J.J.G., Cesar Jr., R.M., Jelinek, H.F., Cree, M.J.: Retinal vessel segmentation using the 2D Gabor wavelet and supervised classification. IEEE Trans. Med. Imag. **25**(9), 1214–1222 (2006)
3. Marin, D., Aquino, A., Gegundez-Arias, M.E., Bravo, J.M.: A new supervised method for blood vessel segmentation in retinal images by using gray-level and moment invariants-based features. IEEE Trans. Med. Imag. **30**, 146–158 (2011)
4. Bekkers, E.J., Duits, R., Berendschot, T., ter Haar Romeny, B.: A multi-orientation analysis approach to retinal vessel tracking. Journal of Mathematical Imaging and Vision, pp. 1–28 (2014)
5. Hoover, A., Kouznetsova, V., Goldbaum, M.: Locating blood vessels in retinal images by piecewise threshold probing of a matched filter response. IEEE Trans. Med. Imag. **19**(3), 203–211 (2000)
6. Al-Rawi, M., Qutaishat, M., Arrar, M.: An improved matched filter for blood vessel detection of digital retinal images. Comput. Biol. Med. **37**, 262–267 (2007)

7. Li, Q., You, J., Zhang, D.: Vessel segmentation and width estimation in retinal images using multiscale production of matched filter responses. Expert Systems with Applications **39**(9), 7600–7610 (2012)
8. Al-Diri, B., Hunter, A., Steel, D.: An active contour model for segmenting and measuring retinal vessels. IEEE Trans. Biomed. Eng. **29**(9), 125–1497 (2009)
9. Krause, M., Alles, R., Burgeth, B., Weickert, J.: Fast retinal vessel analysis. J. Real-Time Image Process, 1–10 (2013). doi:10.1007/s11554-013-0342-5
10. Zhang, B., Zhang, L., Zhang, L., Karray, F.: Retinal vessel extraction by matched filter with first-order derivative of Gaussian. Computers in Biology and Medicine **40**, 438–445 (2010)
11. Azzopardi, G., Strisciuglio, N., Vento, M., Petkov, N.: Trainable COSFIRE filters for vessel delineation with application to retinal images. Med. Image Anal. **19**, 46–57 (2015)
12. Chauduri, S., Chatterjee, S., Katz, N., Nelson, M., Goldbaum, M.: Detection of blood-vessels in retinal images using two-dimensional matched-filters. IEEE Trans. Med. Imag. **8**, 263–269 (1989)
13. Mendonca, A.M., Campilho, A.: Segmentation of retinal blood vessels by combining the detection of centerlines and morphological reconstruction. IEEE Trans. Med. Imag. **25**, 1200–1213 (2006)
14. Zhang, J., Duits, R., Sanguinetti, G., ter Haar Romeny, B.M.: Numerical Approaches for Linear Left-invariant Diffusions on SE(2), their Comparison to Exact Solutions, and their Applications in Retinal Imaging. Accepted by Numerical Mathematics: Theory, Methods and Applications (NM-TMA) **40**, 1–49 (2015). Preprint. arxiv.org/abs/1403.3320
15. Duits, R., Felsberg, M., Granlund, G., ter Haar Romeny., B.M.: Image analysis and reconstruction using a wavelet transform constructed from a reducible representation of the Euclidean motion group. International Journal of Computer Vision **79**(1), 79–102 (2007)
16. Hubel, D.H., Wiesel, T.N.: Receptive fields of single neurons in the cat's striate cortex. The Journal of Physiology **148**, 574–591 (1959)
17. Frangi, A.F., Niessen, W.J., Vincken, K.L., Viergever, M.A.: Multiscale vessel enhancement filtering. In: Wells, W.M., Colchester, A.C.F., Delp, S.L. (eds.) MICCAI 1998. LNCS, vol. 1496, pp. 130–137. Springer, Heidelberg (1998)
18. Lindeberg, T.: Scale-space theory: A basic tool for analysing structures at different scales. Journal of Applied Statistics **21**(2), 224–270 (1994)
19. Foracchia, M., Grisan, E., Ruggeri, A.: Luminosity and contrast normalization in retinal images. Med. Image Anal. **9**(3), 179–190 (2005)
20. Staal, J., Abramoff, M.D., Niemeijer, M., Viergever, M.A., van Ginneken, B.: Ridge-based vessel segmentation in color images of the retina. IEEE Trans. Med. Imag. **23**(4), 501–509 (2004)